

See discussions, stats, and author profiles for this publication at: <https://www.researchgate.net/publication/228812099>

# Molecular Level Friction As Revealed with a Novel Scanning Probe

ARTICLE *in* LANGMUIR · APRIL 1999

Impact Factor: 4.46 · DOI: 10.1021/la981521r

---

CITATIONS

61

---

READS

20

4 AUTHORS, INCLUDING:



**Alan Burns**

University of Houston

**491** PUBLICATIONS **15,834** CITATIONS

SEE PROFILE



**Robert W Carpick**

University of Pennsylvania

**222** PUBLICATIONS **6,368** CITATIONS

SEE PROFILE

# Molecular Level Friction As Revealed with a Novel Scanning Probe

A. R. Burns,\* J. E. Houston, R. W. Carpick, and T. A. Michalske

Surface and Interface Sciences Department, MS 1413, Sandia National Laboratories,  
Albuquerque, New Mexico 87185-1413

Received October 28, 1998. In Final Form: February 19, 1999

Friction at the molecular level is examined with a novel scanning probe microscope that observes the onset of energy dissipation and adhesive forces simultaneously. Friction is monitored by measuring the damped vibrational amplitude of an oscillating probe tip, analogous to shear-force feedback commonly used in near-field scanning optical microscopes. A mechanically stable interfacial force sensor is used to measure normal forces at the tip independently and decoupled from the lateral forces, allowing one to observe friction from the early stages of the purely adhesive tensile regime to the latter stage of repulsive compression. Measurements on model lubricant silane and alkanethiol self-assembled monolayers indicate that friction dramatically increases with the strength of adhesive interactions between the tip and the monolayers. These adhesive interactions occur over an appreciable ( $7 \pm 1$  Å) displacement range, suggesting tensile reorientation of the lubricant chains and subsequent energy losses due to collective chain motion as well as dissipative hydrogen-bond breaking.

## Introduction

Our understanding of friction has advanced considerably in recent years by fundamental studies, both experimentally and computationally, at the molecular level.<sup>1–3</sup> Vibrational energy losses induced by interfacial bond rupture, mechanical deformation, and phonons account for much of the energy dissipation.<sup>2,4</sup> Other channels that have been identified include electronic losses to the substrate.<sup>1</sup> Recently, there has been substantial work on the effects of “model lubricants” on interfacial friction. In particular, self-assembling alkanethiols<sup>5</sup> and silanes<sup>6</sup> have been used extensively because they can be tailored to examine “mechanical” parameters such as chain length, packing density,<sup>3,7</sup> and cross-linking,<sup>8</sup> as well as “chemical” parameters such as the strength of adhesive molecular interaction.<sup>9,10</sup> Mechanical and chemical effects can be difficult to separate for the chainlike silanes and alkanethiols, however, because they are anchored firmly, relative to more fluid lubricants, to one or both contacting surfaces by their headgroups.

The effects of model lubricants on the relationship between friction and load have been studied with the surface forces apparatus (SFA)<sup>4,11</sup> and the scanning probe atomic force microscope (AFM).<sup>3,9,10</sup> Both the spring-based SFA and cantilever-based AFM exhibit mechanical in-

stabilities when making (“jump to contact”) and breaking (“pull off”) interfacial contacts in the common situation where the attractive force gradient exceeds the respective spring constants. The problem is exacerbated when chemical modification leads to stronger adhesive interactions at the interface and hence much greater force gradients.<sup>9,10</sup> On approach, the jump-to-contact instability can completely obscure the depth of the initial molecular adhesive interaction. Mechanical impact resulting from the jump-to-contact may also significantly alter the character of the adhesive interface and thus affect the forces commonly measured at pull-off. This issue is made more explicit by the observation of adhesion hysteresis, i.e., when the interfacial adhesion energy is greater at pull-off than that measured during approach.<sup>4,12</sup> Thus the exact relation between friction, interfacial adhesion, and load is hidden since friction forces are generally measured only in the repulsive regime of the contact, or for a limited range preceding pull-off that has both repulsive and attractive components.<sup>13</sup> Finally, the finite mechanical coupling between the normal and lateral force sensing modes of a typical AFM cantilever<sup>14</sup> must also be taken into account in the analysis of friction-load relations.

As noted above, the relationship between friction and adhesion is not clear-cut, since many factors are involved in energy dissipation. It would be beneficial to know in more detail the relative importance of adhesion with regard to load and the structure of the materials in the contact. In this paper, we approach that problem by describing a new way of examining frictional forces over the *entire* adhesive interaction between a scanning probe tip and the sample surface that not only avoids the inherent mechanical instabilities of spring-based sensors, but also completely decouples normal and lateral force sensors. The experimental method is based on bringing together the techniques of shear-force microscopy<sup>15,16</sup> and

\* To whom correspondence should be addressed. E-mail: aburns@sandia.gov.

- (1) Krim, J. *Sci. Am.* **1996**, 275, 74.
- (2) Bhushan, B.; Israelachvili, J. N.; Landman, U. *Nature* **1995**, 374, 607.
- (3) Carpick, R. W.; Salmeron, M. *Chem. Rev.* **1997**, 97, 1163.
- (4) Israelachvili, J. N. In *Handbook of Micro/Nanotribology*; Bhushan, B., Ed.; Chemical Rubber Co.: Boca Raton, FL, 1995; p 267.
- (5) Dubois, L. H.; Nuzzo, R. G. *Annu. Rev. Phys. Chem.* **1992**, 43, 437.
- (6) Sagiv, J. *J. Am. Chem. Soc.* **1980**, 102, 92.
- (7) Lio, A.; Charych, D. H.; Salmeron, M. *J. Phys. Chem. B* **1997**, 101, 3800.
- (8) Shinn, N. D.; Kim, T.; Daly, C.; Mayer, T. M.; Crooks, R. M.; Michalske, T. A. *Langmuir*, in press.
- (9) Frisbie, C. D.; Rozsnyai, L. F.; Noy, A.; Wrigton, M. S.; Lieber, C. M. *Science* **1994**, 265, 2071.
- (10) Noy, A.; Vezennov, D. V.; Lieber, C. M. *Annu. Rev. Mater. Sci.* **1997**, 27, 381.
- (11) Peanasky, J.; Schneider, H.; Granick, S. *Langmuir* **1995**, 11, 953.

- (12) Burnham, N. A., et al. *Nanotechnology* **1997**, 8, 67.
- (13) Horn, R. G.; Israelachvili, J. N.; Pribac, F. *J. Colloid Interface Sci.* **1986**, 115, 480.
- (14) Ogletree, D. F.; Carpick, R. W.; Salmeron, M. *Rev. Sci. Instrum.* **1996**, 67, 3298–3306.
- (15) Betzig, E.; Finn, P. L.; Weiner, J. S. *Appl. Phys. Lett.* **1992**, 60, 2484.

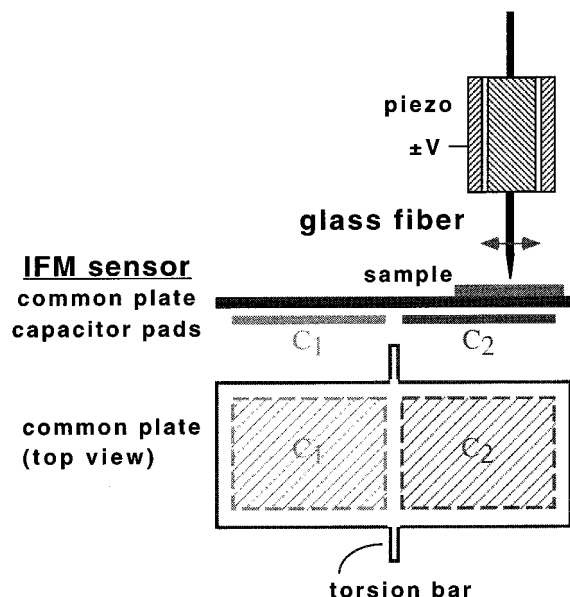


**Figure 1.** Schematic of experiment. A vibrating glass fiber with a tip diameter  $<100$  nm is brought into contact with a sample resting on an IFM sensor. The sensor measures the adhesive (negative loads) and repulsive (positive loads) forces on the tip by maintaining an electrostatic balance of two capacitances  $C_1$  and  $C_2$ , formed by the common plate and identical gold pads fixed on a glass substrate (not shown).

interfacial force microscopy (IFM).<sup>17,18</sup> With this arrangement, frictional forces acting to dampen the tip's lateral motion are monitored independently as a function of both positive (compressive) and negative (adhesive) loads. Thus the adhesive nature of friction at the earliest stages of contact can be clearly characterized.<sup>19</sup> Initial results with a fluorosilane adsorbed on silicon and two alkanethiols with chemically distinct tail groups adsorbed on gold will be discussed. (Fluorosilanes are used to reduce friction and adhesion in silicon micromechanical structures.<sup>20</sup>) We will show evidence that strong adhesive forces due to hydrogen bonding lead to frictional loss not only due to dissipative intermolecular forces (e.g., bond breaking) at the contact interface, but also in part to tensile deformation (reorientation) and collective motion of the hydrocarbon chains.

### Experimental Section

A schematic of the experimental arrangement is shown in Figure 1. It consists of a bare glass fiber mounted on a small "dither" piezo tube, which vibrates the fiber laterally, and a sample resting on an IFM sensor.<sup>17</sup> The sensor is mounted on a second, larger piezo (not shown) that is used for controlling the tip-sample distance and for scanning. The diameter of the glass probe tip is reduced to  $<100$  nm by using a commercial puller (Sutter Instruments). An IFM sensor consists of a teeter-totter-like common plate of a differential capacitor suspended by torsion bars above two identical gold pads fixed in a glass substrate, creating capacitances  $C_1$  and  $C_2$  in Figure 1. Details concerning operation of the sensor may be found elsewhere<sup>17,21</sup> and are only briefly summarized here. The position of the common plate is determined by an rf bridge circuit and is initially balanced by

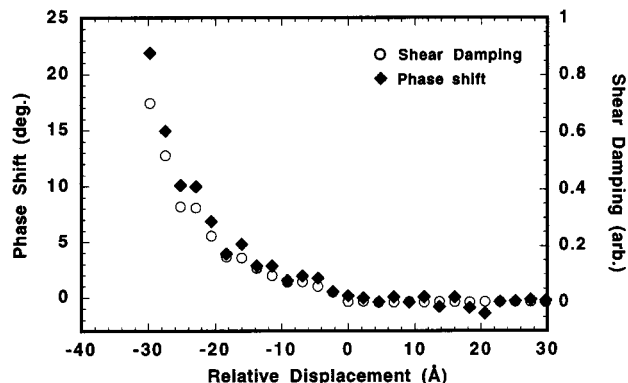


**Figure 2.** Shear damping and phase shift vs displacement between vibrating ( $\pm 12$  nm) bare glass tip and a monolayer of  $\text{CF}_3(\text{CF}_2)_5(\text{CH}_2)_2\text{Si}(\text{Cl})_3$  (FTS) on silicon. Zero displacement is arbitrarily set at the point of initial friction.

static voltages applied to the capacitor pads. The sensor is then placed under proportional integral derivative feedback control by a circuit that supplies voltages to one pad to counteract any error signal due to normal forces acting on the fiber tip. The normal force can be directly calculated with reasonable accuracy and precision ( $\pm 20\%$ ) from the feedback voltage, the capacitances, and the static voltages, or it can be directly calibrated (with greater accuracy and precision) using a laboratory microbalance.<sup>21</sup> Unlike AFM cantilevers, the sensor is mechanically stable, noncompliant, and completely decoupled from the lateral motion of the tip. (Such a noncompliant device is often referred to as a "fixed grips" apparatus.<sup>22</sup>)

As in most near-field scanning optical microscopy configurations<sup>23</sup> employing "shear-force" feedback,<sup>15,16</sup> the optical fiber typically has a mechanical resonance at 25–50 kHz (for 2–3 mm lengths), and a  $Q$  factor of  $\sim 100$  before contact. The amplitude of the lateral motion is determined by  $A_{\text{piezo}} Q$ , where  $A_{\text{piezo}}$  is the dither piezo drive amplitude (see Appendix). The dither piezo is in turn driven by a sinusoidal voltage applied to one of four quadrants. Fiber motion induces voltages on the piezo, which is detected on the remaining quadrants by a phase-sensitive lock-in amplifier.<sup>24</sup> A large, constant background is present due to the dither piezo driving motion, but this is easily subtracted. Unless otherwise stated, we use an initial "free" lateral displacement amplitude of  $\sim 12$  nm, and we are able to detect tip amplitudes  $<1$  nm upon contact with the sample. Attenuation of the fiber amplitude upon interaction of the probe tip with the surface is the basis for our friction measurements and for shear-force feedback, which allows the tip to be scanned over the surface without damage to tip or surface. The shear force damping (friction force) is proportional to the quantity  $(1 - V/V_0)$ , where  $V$  is the attenuated signal at a given displacement amplitude and  $V_0$  is the unattenuated signal due to the free lateral displacement amplitude prior to contact (see Appendix). For the initial 12 nm free amplitude, we estimate that the frictional force at complete damping is 18 nN (see Appendix). By keeping the initial free amplitude constant, we in effect use the *same range of friction force* (0–18 nN) for all the experiments discussed here.

An example of shear force damping vs displacement is shown in Figure 2, where zero displacement is arbitrarily set to be the point where friction is first detected. Independent piezo calibration was performed against a known 50 Å feature; we estimate the displacement is accurate to within 15%. Also shown in Figure 2 is the corresponding phase shift of the tip amplitude vs displacement, where  $V_0$  is arbitrarily set by the lock-in amplifier to have a zero phase shift. We see that the phase shift correlates very closely with the shear damping (see Appendix). The maximum phase shift observed at 90% attenuation of the initial 12 nm amplitude is  $<25^\circ$ , thus the quantity  $x = V \cos(\theta)$  measured by the lock-in is to a good approximation equal to the amplitude

(16) Toledo-Crow, R.; Yang, P. C.; Chen, Y.; Vaez-Iravani, M. *Appl. Phys. Lett.* **1992**, *60*, 2957.

(17) Joyce, S. A.; Houston, J. E. *Rev. Sci. Instrum.* **1991**, *62*, 710.

(18) Thomas, R. C.; Houston, J. E.; Crooks, R. M.; Kim, T.; Michalske, T. A. *J. Am. Chem. Soc.* **1995**, *117*, 3830.

(19) Burns, A. R.; Houston, J. E.; Carpick, R. W.; Michalske, T. A. *Phys. Rev. Lett.* **1999**, *82*, 1181.

(20) Maboudian, R.; Howe, R. T. *J. Vac. Sci. Technol. B* **1997**, *15*, 1.

(21) Warren, O. L.; Graham, J. F.; Norton, P. R. *Rev. Sci. Instrum.* **1997**, *68*, 4124.

(22) Greenwood, J. A. *Proc. R. Soc. London A* **1997**, *453*, 1277.

(23) Paesler, M. A.; Moyer, P. J. *Near Field Optics Theory, Instrumentation, and Applications*; John Wiley & Sons: New York, 1996.

(24) Barentz, J.; Hollricher, O.; Marti, O. *Rev. Sci. Instrum.* **1996**, *67*, 1912.

$V$  for the whole attenuation range. It is important to note that due to the large background created by the dither piezo, the apparent phase shift measured directly with the lock-in is very small.<sup>24</sup> The actual phase shift vs displacement shown in Figure 2 was obtained by independent measurement of the lock-in signals  $x = V \cos(\theta)$  and  $y = V \sin(\theta)$ .

Three different samples were prepared. The first consisted of a fluorinated silane,  $\text{CF}_3(\text{CF}_2)_5(\text{CH}_2)_2\text{Si}(\text{Cl})_3$  (hereafter denoted FTS), vapor-deposited under anhydrous conditions onto a silicon (100) substrate held at 50 °C. The substrate was previously cleaned and hydroxylated in a 7:3  $\text{H}_2\text{SO}_4/\text{H}_2\text{O}_2$  solution and dried under nitrogen. From ellipsometry measurements, it was verified that no more than one monolayer was deposited. The second and third samples were self-assembled molecular monolayers of two alkanethiols having the same chain length but differing tail groups:  $\text{CH}_3(\text{CH}_2)_{11}\text{SH}$  (hereafter denoted  $\text{CH}_3$ -thiol), and  $\text{COOH}(\text{CH}_2)_{11}\text{SH}$  (hereafter denoted  $\text{COOH}$ -thiol). The substrates were 100 nm thick Au films, vacuum evaporated onto a 10 nm thick film of Cr on clean silicon (100). The self-assembly took place in 1 mM thiol solutions in ethanol over 24 h at room temperature. The chemistry of the bare glass tip was not modified; thus the native OH groups interact with the molecular monolayers.

All experiments were done immediately following sample preparation and under an atmosphere of filtered, dry nitrogen (relative humidity <8%). Water is expected to be present in monolayer quantities under these conditions; however, no capillary condensation was observed. Control of the microscope and data acquisition are through home-built electronics and software. The same bare glass tip was used throughout the experiments discussed below. Charging precludes scanning electron microscopy (SEM) analysis of bare tip shapes and sizes. However, SEM analysis has been performed on dozens of tips created under identical pulling conditions and coated with a known thickness of Al. We have found that the tips are blunt (flat), with a radius that varies from 30 to 50 nm; model tip shapes resembling the SEM images will be discussed in the next section.

## Results and Discussion

We show in Figure 3 the simultaneous response of the IFM normal force sensor together with the lateral shear damping (friction) when the tip approaches each of the three different samples. From top to bottom, the samples are FTS,  $\text{CH}_3$ -thiol, and  $\text{COOH}$ -thiol. The same tip and sensor are used throughout, and the same approach displacement rate of 2.5 Å/s is used. The experiment is controlled by the degree of lateral damping; i.e., when the attenuation becomes greater than a preset value (80% of the undamped 12 nm amplitude), the tip is withdrawn at the same rate as the approach. (For the sake of clarity, we do not show the withdrawal curves). As mentioned in the previous section, the same range of friction is explored in each case. We have also, like Figure 2, arbitrarily set zero in the displacement axis to be the point where the damping (friction) begins.

In the top panel of Figure 3, we see that as the shear force damping of the tip motion by interaction with the FTS monolayer begins, the IFM sensor indicates a negative load. The negative load reaches a maximum of  $-160$  nN at  $\sim 15\%$  damping and  $-6 \pm 1$  Å relative displacement. This load correlates with the "pull-off" force in the absence of adhesive hysteresis. Thus it is clear that the initial shear force damping is due to a negative load created by *adhesive* forces on the probe tip. It is not until the lateral amplitude is reduced by  $\sim 60\%$  of its initial free value that the load becomes positive, indicating a net *compressive* interaction. As the load increases from the  $-160$  nN value, the monolayer and substrate are being compressed. The force-displacement relation in this  $\sim 18$  Å compressive regime is consistent with the Johnson-Kendall-Roberts

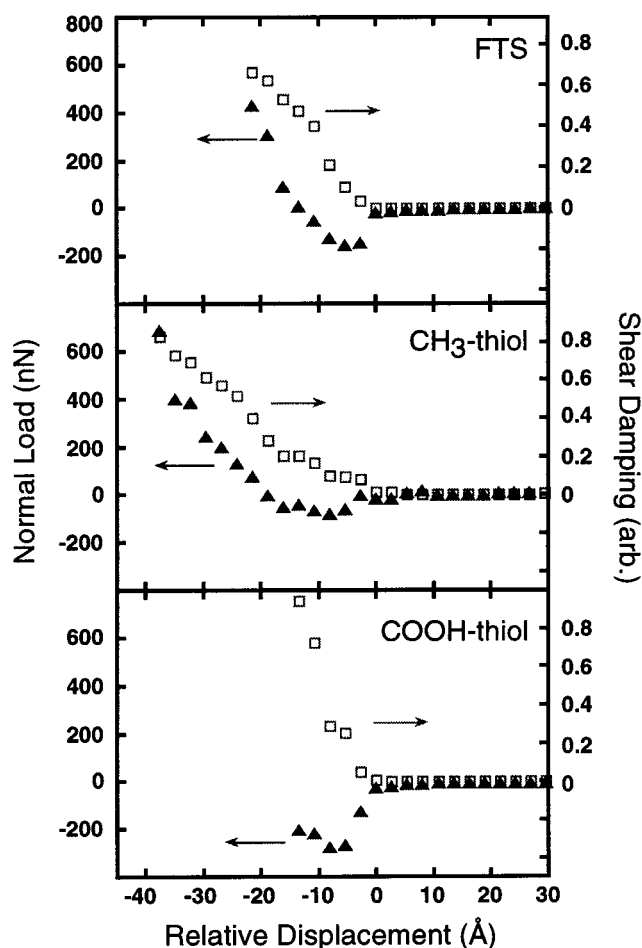


**Figure 3.** Simultaneous shear damping of tip lateral motion (□) and normal forces (▲) on tip acquired for approach to FTS (top),  $\text{CH}_3$ -thiol (middle), and  $\text{COOH}$ -thiol (bottom) self-assembled monolayers. Zero displacement is arbitrarily set at the point of initial friction.

(JKR) model of elastic adhesive contacts<sup>25</sup> discussed further below. Indeed, a JKR force displacement fit to the compression data provides an effective Young's Modulus of  $12.9 \pm 3$  GPa for this system. For self-consistency, we use this value in the friction-load relation discussed below; however, we caution that it was clearly measured under small loads and should not be compared to stiffer values measured with higher loads. Thus the mechanism(s) of lateral motion damping can have both adhesive (tensile) and repulsive (compressive) components; however, it is clear that the first stage of friction is caused by adhesive forces at the monolayer-tip contact interface before any compression of the film and substrate occurs.

We can vary the strength of the initial adhesive forces in a controlled way by examining the  $\text{CH}_3$ -thiol and  $\text{COOH}$ -thiol monolayers. In the middle panel of Figure 3, we see from the initial IFM response to the tip interaction with the  $\text{CH}_3$ -thiol that there is a weak adhesive interaction which reaches a negative load maximum of approximately  $-100$  nN, at a relative displacement of  $-7 \pm 1$  Å. As the tip continues the approach, the adhesive interaction is overwhelmed by stronger repulsive forces that compress the  $\text{CH}_3$ -thiol monolayer and gold substrate. Thus most of the shear damping in the  $\text{CH}_3$ -thiol case is due to compressive (repulsive) forces on the tip, with a relatively small contribution from adhesive forces. An effective

(25) Johnson, K. L.; Kendall, K.; Roberts, A. D. *Proc. R. Soc. London A* **1971**, *324*, 301.



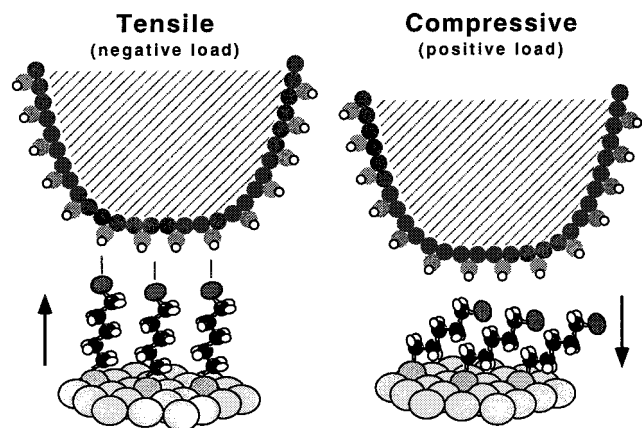


**Figure 4.** Highly schematic representation (not to scale) of glass tip interaction with self-assembled thiols and silanes that are anchored to substrate. The upward arrow at left depicts the tensile molecular deformation under negative loads that includes a reorientation of the thiol chains from a  $\sim 30^\circ$  tilt to a  $0^\circ$  tilt. The downward arrow at right depicts compressive deformation of the chains under positive loads. The extent of tensile stress, and ultimately that of friction in the lateral motion of the tip, is directly related to the strength of the adhesive interaction between the tail groups and the OH groups on the tip.

Young's modulus of  $8.0 \pm 1$  GPa is deduced for this system from the JKR force–displacement fit over the  $\sim 32$  Å compressive region. Once again, this modulus is used below for self-consistency and should not be compared to values obtained under much higher loads.

In remarkable contrast to the  $\text{CH}_3$ -thiol, it is seen at the bottom of Figure 3 that the tip interaction with the  $\text{COOH}$ -thiol is almost purely adhesive; the tip motion is completely damped before appreciable repulsive compression can occur. In fact, the steep rise in friction with displacement and negative load suggests that a significant fraction of  $\text{COOH}$ -thiol chains undergo tensile adhesive interaction with the glass probe tip and collectively bring it to a halt. Other channels of energy dissipation thus come into play. Given the mechanical coupling of the molecular chains to substrate, the collective motion of the chains should act as an efficient channel for vibrational energy loss to the substrate. Also, making and breaking adhesive bonds can result in dissipative molecular motion and disordering, including chain entanglement and gauche defects.<sup>26</sup>

To summarize our observations so far, we note a considerable difference in the mechanisms of shear force damping strictly on the basis of adhesive interaction strength between the monolayers and the glass probe tip. The data from the FTS monolayer appears to exhibit both significant adhesive and compressive behavior. As discussed below where we consider the nature of the adhesive interactions, the stronger adhesion of the FTS monolayer relative to the  $\text{CH}_3$ -thiol is not expected given the low surface energy of fluorocarbon films.<sup>27,28</sup> The two “extremes” of monolayer–tip interactions that result in energy dissipation, indicated by the  $\text{CH}_3$ -thiol and  $\text{COOH}$ -thiol data, are schematically illustrated in Figure 4. On the left we show the strong tensile adhesive interaction of the  $\text{COOH}$ -thiols with the probe tip, and on the right we show the compressive interaction with the  $\text{CH}_3$ -thiols.

For a given molecular film–tip interaction, friction will contain varying contributions from both adhesive (tensile) and compressive interactions as a function of load.

In each of the IFM data sets in Figure 3 we see that the tensile, adhesive interaction between the tip and the tail groups extends from zero to  $\sim -7 \pm 1$  Å relative displacement. Long-range attractive interactions out of contact have been observed previously in normal force displacement curves,<sup>18,29,30</sup> but we cannot attribute the simultaneous onset of friction to noncontact long-range forces. Excitation of substrate phonons and electrons has been identified as possible noncontact energy dissipation channels;<sup>31,32</sup> however, such forces are estimated to be considerably smaller than those lateral forces discussed here. Thus we must account for the  $\sim -7 \pm 1$  Å range of the tensile interaction in terms of close-range molecular forces, i.e., adhesion. We can account for  $\sim 3$  Å of the contact range through the motion of the thiol (and, possibly, the silane) chains from the initial  $30^\circ$  tilt (in the case of the thiols) to a  $0^\circ$  upright position. In other words, the displacement range suggests that many hydrocarbon chains “stand up” from their  $30^\circ$  tilt<sup>5</sup> to meet the probe (see Figure 4). Therefore, noncontact attractive forces (which eventually become full hydrogen-bonding and/or van der Waals interactions) reorient the molecules at some critical displacement before friction is observed. Unfortunately, this IFM sensor is not sensitive enough to detect these noncontact forces prior to the observation of friction. As soon as the adhesive tensile contact is created, friction and negative loading are observed. Clearly these effects are more pronounced for the  $\text{COOH}$ -thiol. Given the weak tensile interaction, some of the  $\sim 18$  Å long  $\text{CH}_3$ -thiol chains appear to stand up as well; but they are unable to significantly dampen the tip's lateral motion because of the relatively weak adhesion. The  $\sim 12$  Å long FTS chains also should undergo tensile deformation given the significant observed negative load, although the initial tilt angle of the chains is unknown.

Using the JKR analysis, we have calculated that an additional  $1-2$  Å displacement in the initial negative load region can be associated with tensile deformation of the substrates and tip.<sup>22</sup> The remaining  $2-3$  Å of the total apparent  $7 \pm 1$  Å tensile region could be due to surface roughness over the  $\pm 12$  nm lateral motion. For the densely packed and ordered thiols, a tensile deformation of the layer requires overcoming some of the cohesive chain–chain van der Waals forces. This should be more difficult to do for the  $\text{CH}_3$ -thiol chains, relative to the  $\text{COOH}$ -thiol chains, because of the weaker forces driving the deformation. (The degree of initial ordering in the  $\text{CH}_3$ -thiol and  $\text{COOH}$ -thiol monolayers is expected to be the same.<sup>33</sup>) Since cohesive forces increase with chain length, the likelihood of  $\text{CH}_3$ -terminated chains undergoing tensile deformation should decrease with increasing chain length. This may explain, in part, the AFM observation of decreasing friction force with chain length.<sup>7</sup>

One concern pertaining to the shear force displacement range is that the tip may be slightly tilted with respect to the samples; this would result in a nonuniform surface interaction dominated by one turning point of its motion.<sup>34</sup>

(26) Baljon, A. R. C.; Robbins, M. O. *Science* **1996**, *271*, 482.

(27) Burnham, N. A.; Dominguez, D. D.; Mowery, R. L.; Colton, R. *J. Phys. Rev. Lett.* **1990**, *64*, 1931.

(28) Israelachvili, J. N. *Intermolecular and Surface Forces*, 2nd ed.; Academic Press: London, 1992.

(29) Blackman, G. S.; Mate, C. M.; Philpott, M. R. *Phys. Rev. Lett.* **1990**, *65*, 2270.

(30) Burnham, N. A.; Colton, R. J.; Pollock, H. M. *Nanotechnology* **1993**, *4*, 64.

(31) Gerlach, E. *Phys. Stat. Solidi B* **1993**, *176*, 365.

(32) Krim, J. *Comments Condens. Mater. Phys.* **1995**, *17*, 263.

(33) Nuzzo, R. G.; Dubois, L. H.; Allara, D. L. *J. Am. Chem. Soc.* **1990**, *112*, 558.

(34) Gregor, M. J.; Blome, P. G.; Schöfer, J.; Ulbrich, R. G. *Appl. Phys. Lett.* **1996**, *68*, 307.

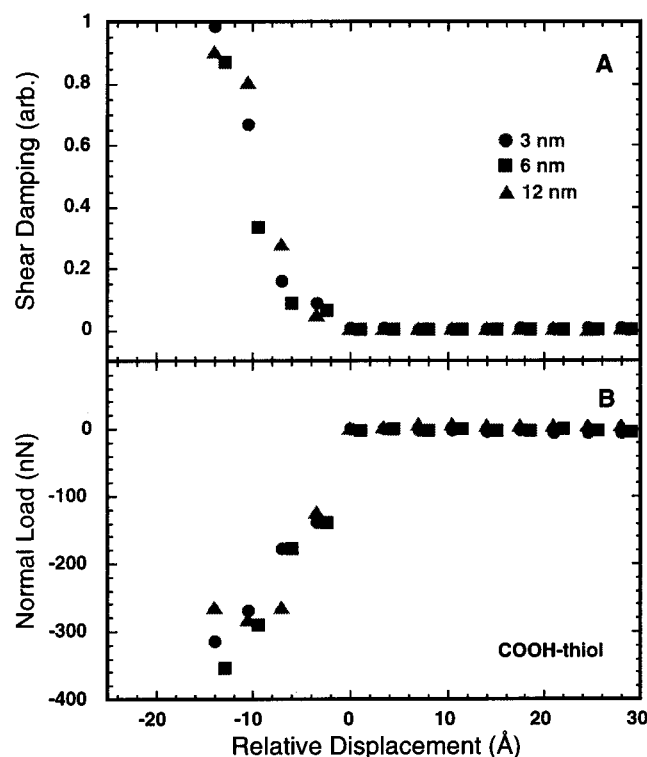


**Figure 5.** (A) Shear damping for various free, initial tip amplitudes: (●) 3 nm, (■) 6 nm, (▲) 12 nm. (B) Simultaneous IFM signals for shear force damping. The substrate is covered with COOH-thiol.

When this occurs, the displacement range of shear force damping increases with free, initial lateral amplitude.<sup>34</sup> In our case, we see in Figure 5A that as the free amplitude of the tip's lateral motion is reduced from 12 to 3 nm, there is no change in the displacement range of the shear force damping as it approaches the COOH-thiol surface. Thus we can conclude that the displacement range for the  $\pm 12$  nm data is due solely to laterally uniform adhesive interactions discussed above. The simultaneous IFM signals in Figure 5B support this conclusion by indicating strong negative loads for each amplitude at comparable displacements. The strong potential well of the COOH-thiol–tip interaction is responsible for the steep and amplitude-independent displacement range of the shear forces. Given a high enough initial amplitude ( $\gg 12$  nm) to overcome the potential well, the displacement range would increase due to monolayer and substrate compression under positive loads. Indeed, when the shear force amplitude dependence is measured for the CH<sub>3</sub>-thiol, higher loads (stronger repulsive forces) over slightly longer displacement ranges are required to dampen the  $\pm 12$  nm initial amplitude relative to the  $\pm 3$  nm initial amplitude.

The corresponding withdrawal curves for Figure 3 (not shown) usually exhibit some adhesive hysteresis with stronger adhesive forces than the approach curves. The causes of adhesive hysteresis are poorly understood, but are generally associated with irreversible mechanical, chemical, and/or structural effects such as disordering<sup>28,35</sup> that goes beyond the scope of this study. The clear advantage of the present technique is that we can examine the adhesive interaction during approach.

"Chemical force microscopy" has been identified as a means to utilize differences in adhesive forces as a contrast mechanism in AFM imaging.<sup>9,10</sup> The results discussed

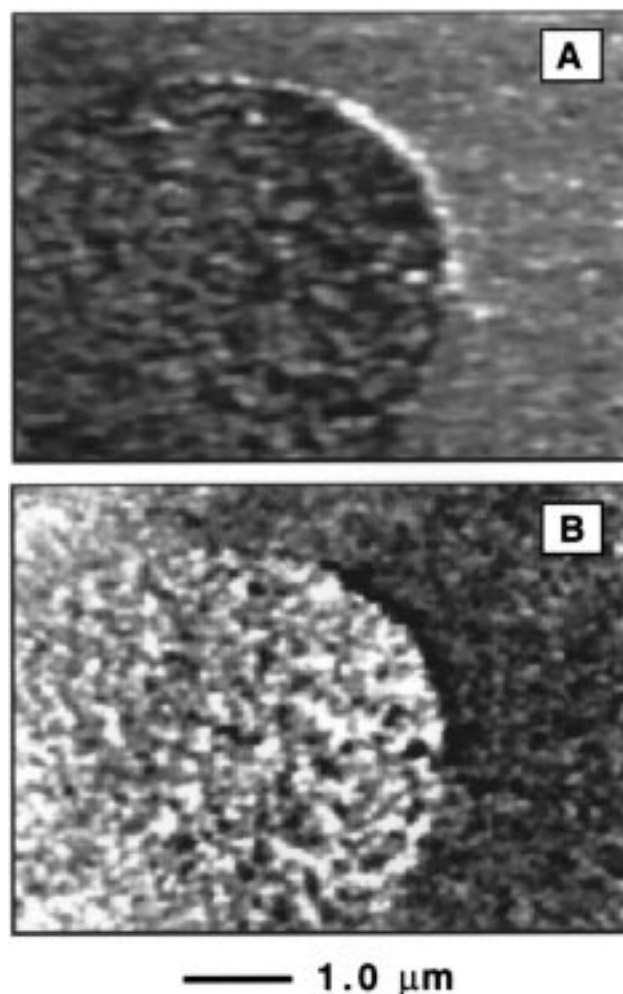


**Figure 6.** Simultaneous 6.0  $\mu\text{m}$  shear-force feedback (A) and IFM normal force (B) images of a patterned thiol monolayer. Inside the circle is CH<sub>3</sub>-thiol, and outside the circle is COOH-thiol. In (A), bright (dark) areas indicate more (less) tip withdrawal by the scanning piezo to maintain constant shear-force damping, whereas in (B), the bright (dark) areas indicate weaker (stronger) adhesive normal forces.

above are consistent with the AFM contrast observed for the same thiols. However, it is important to note that due to the cantilever snap-to-contact instability, the AFM lateral force studies are restricted to *repulsive* contact or to the limited range of adhesive and repulsive interactions<sup>13</sup> prior to pull-off. We now demonstrate that the difference in purely adhesive forces discussed above can also be resolved in images. We prepared a sample having a pattern of two thiols created by the technique of microcontact printing.<sup>36</sup> A poly(dimethylsiloxane) stamp having 5.0  $\mu\text{m}$  circles is "inked" with the CH<sub>3</sub>-thiol solution (1 mM in ethanol) and applied to a clean Au-covered substrate for two minutes as discussed in ref 36; unstamped areas are then covered with the COOH-thiol by immersion in the 1 mM ethanol solution for 10 min. In Figure 6A, we show a 6.0  $\mu\text{m}$  image of the feedback signal required to maintain a constant shear force damping of 10%, which is in the region of negative load (tensile) normal forces. When the tip is scanned from the CH<sub>3</sub>-thiol region inside the circle to the COOH-thiol region outside, it must withdraw to maintain 10% shear damping under the stronger and steeper adhesive interaction. Thus the areas outside the circles in Figure 6A are "higher" (brighter).

(35) Israelachvili, J. N.; Chen, Y.-L.; Yoshizawa, H. *J. Adhes. Sci. Technol.* **1994**, *8*, 1231.

(36) Kumar, A.; Whitesides, G. M. *Appl. Phys. Lett.* **1993**, *63*, 2002.

The normal force signal from the IFM acquired simultaneously during the scan is shown in Figure 6B. The IFM image is reversed relative to Figure 6A because the COOH-thiol area produces a more negative (tensile) signal relative to the CH<sub>3</sub>-thiol area (see Figure 3). Thus, it is possible to map adhesive bond strengths in the *tensile regime* with this method. It is also apparent from this experiment that shear-force feedback images commonly used to reveal "topologies" in near-field scanning optical microscopy<sup>15,16</sup> can be misleading when different chemical constituents are present on the substrate.

Examination of the friction-load relation can yield considerable insight into the molecular mechanics of wearless friction and can yield important parameters such as the work of adhesion and the shear strength for a given interface. It was shown with the SFA<sup>4,37</sup> that friction at low loads can be analyzed with the JKR<sup>25</sup> model of adhesive elastic contacts, which predicts the dependence of contact area upon the applied load, if one assumes that friction is proportional to the contact area through a constant shear strength (eq 1). The SFA technique has the advantage of measuring the contact area directly, whereas scanning probes do not. Despite this limitation, numerous AFM studies have successfully demonstrated that friction-load relations do reflect molecular properties such as chain length, molecular packing, and tail group chemical identity.<sup>7,38,39</sup> Carpick et al.<sup>3,40</sup> have recently shown that the friction-load relation of an AFM single asperity contact can, in fact, be analyzed within the JKR formalism by once again assuming friction is proportional to contact area. For a parabolic tip-surface contact, the JKR relation of friction  $F$ , load  $L$ , and contact  $A$  is given by eq 1:

$$F = \tau A = \tau \pi \left\{ \frac{R}{K} [L + 3\pi R\gamma + [6\pi R\gamma L + (3\pi R\gamma)^2]^{1/2}] \right\}^{2/3} \quad (1)$$

where

$$K = \frac{4}{3} \left( \frac{1 - \nu_1^2}{E_1} + \frac{1 - \nu_2^2}{E_2} \right)^{-1} \quad (2)$$

and where  $R$  is the tip radius,  $\tau$  is the shear strength which is assumed to be constant with load, and  $\gamma$  is the adhesion energy per unit area. The reduced modulus  $K$  of the two materials in contact (eq 2) is a function of the respective Young's moduli ( $E_1$ ,  $E_2$ ) and Poisson ratios ( $\nu_1$ ,  $\nu_2$ ) of the tip and sample. In our particular case,  $E_2 \approx 70$  MPa and  $\nu_2 = 0.4$  for glass;<sup>41</sup> from our load-displacement data,  $E_1 \approx 13$  MPa for the silane-covered silicon surface and  $E_1 \approx 8$  MPa for the thiol monolayers on Au. If we assume that  $\nu_1 \approx 0.4$  for the hydrocarbon films, then  $K = 17$  MPa for the silane surface, and  $K = 11$  MPa for the thiol surfaces. If  $R$  is known, a plot of friction vs load can be used to determine both constants  $\gamma$  and  $\tau$ . Extensions to eq 1 were developed by ref 40 to accommodate various tip shapes from parabolic to blunt. For an axisymmetric tip approximated with height profile  $z = cr^n$ , where  $c$  is a constant (see Figure 7), we have from ref 40 the load

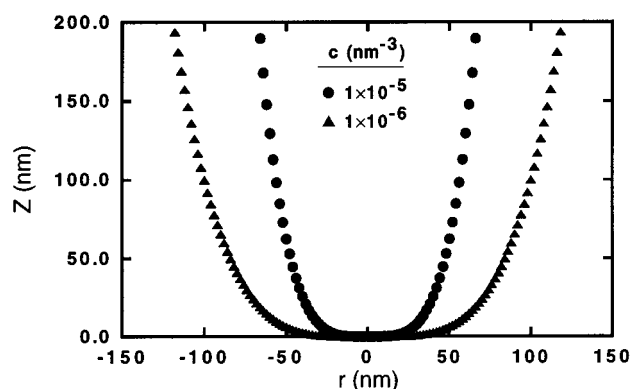


**Figure 7.** Plots of  $z = cr^4$  where  $c = 10^{-5}$  and  $10^{-6} \text{ nm}^{-3}$ , which most closely resemble the blunt glass tip shape used in the experiments.

relation

$$L = -(6\pi\gamma K)^{1/2} (A/\pi)^{3/4} + (3/2) K c n \Psi (A/\pi)^{(n+1)/2} \quad (3)$$

where  $\Psi$  is a constant which depends on  $n$ . A corresponding equation relating displacement and contact area can be derived. The height profile which gives the best approximation to our blunt glass fiber tip shapes and dimensions (based on SEM imaging) is  $z = cr^4$ , which is shown in Figure 7 for  $c = 10^{-6}$  and  $10^{-5} \text{ nm}^{-3}$ . Thus, with  $n = 4$ , we have  $\Psi = 8/15$ <sup>40</sup> and the following relations for load and displacement ( $\delta$ ) respectively:

$$L = -(6\pi\gamma K)^{1/2} (A/\pi)^{3/4} + (16/5) K c (A/\pi)^{5/2} \quad (4)$$

$$\delta = -(8\pi\gamma/3K)^{1/2} (A/\pi)^{1/4} + (8/3) c (A/\pi)^2 \quad (5)$$

The value for  $c$  is not adjustable for a well-characterized tip. However, uncertainty in our tip shapes forces us to fit the  $F(=\tau A)$ ,  $L$  data to eq 4 for several values of  $c$ , and we find that  $c = 10^{-5} \text{ nm}^{-3}$  gives the best results. The determination of the reduced elastic modulus  $K$  mentioned previously involved numerically solving eq 4 and eq 5 simultaneously to eliminate  $A$  and fitting this relation to the load-displacement data in Figure 3.

Figure 8 shows the best fits of eq 4 to the same data that is plotted in Figure 3. The fitting was done by parametrizing eq 4 in terms of the maximum negative load, or critical load  $L_c$ , and the corresponding critical friction  $F_c$  at this load, as discussed in detail in ref 40. From this, one can determine the critical contact area ( $A_c$ ), the interfacial adhesion energy ( $\gamma$ ), and the shear strength ( $\tau$ ).<sup>40</sup> Since we estimate the maximum shear force at 100% lateral damping to be approximately 18 nN (see Appendix), we see for example at the top of Figure 8 that for  $L_c = -160$  nN,  $F_c \approx 0.25 \times 18 \text{ nN} = 4.5 \text{ nN}$ . A summary of the average adhesion energies ( $\gamma$ ), shear strength values ( $\tau$ ), critical loads ( $L_c$ ), etc., over many data sets for each of the three different interfaces is given in Table 1. It should be noted that the small values of  $A_c$  ( $\sim 400 \text{ nm}^2$ ), relative to the full tip geometry, are not unexpected given unresolved tip asperities and surface roughness.

For the CH<sub>3</sub>-thiol we obtain  $\gamma$  and  $\tau$  values which are in very close agreement with purely van der Waals-type molecular interactions.<sup>3,4,18,28</sup> As expected, the COOH-thiol tip interaction has a much higher adhesion energy than that for the CH<sub>3</sub>-thiol. If we subtract the 50 mJ/m<sup>2</sup> van der Waals contribution from 449 mJ/m<sup>2</sup>, as suggested by Fowkes,<sup>42</sup> the result is close to the adhesive energy

(37) Homola, A. M.; Israelachvili, J. N.; Gee, M. L.; McGuiggan, P. M. *J. Tribol.* **1989**, *111*, 675.

(38) Green, J.-B. D.; McDermott, M. T.; Porter, M. D.; Siperko, L. M. *J. Phys. Chem.* **1995**, *99*, 10960.

(39) McDermott, M. T.; Green, J.-B. D.; Porter, M. D. *Langmuir* **1997**, *13*, 2505.

(40) Carpick, R. W.; Agrait, N.; Ogletree, D. F.; Salmeron, M. *J. Vac. Sci. Technol. B* **1996**, *14*, 1289.

(41) Muramatsu, H.; Chiba, N.; Fujihira, M. *Appl. Phys. Lett.* **1997**, *71*, 2061.

(42) Fowkes, F. M. *J. Phys. Chem.* **1962**, *66*, 382.



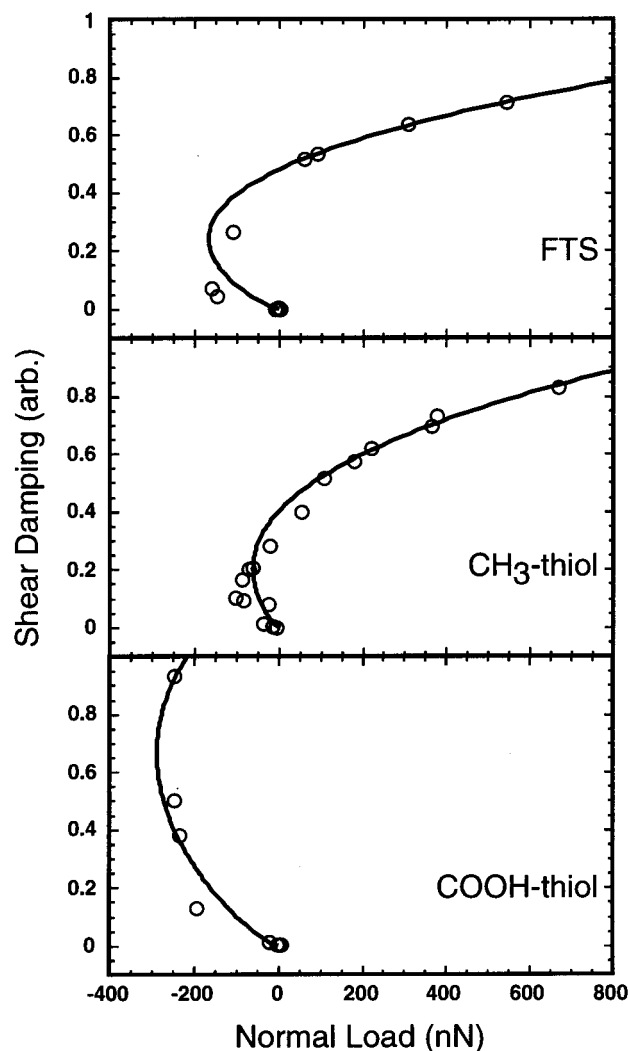


**Figure 8.** Johnson–Kendall–Roberts (JKR) fits to shear damping (friction) vs normal load for the FTS (top), CH<sub>3</sub>-thiol (middle), and COOH-thiol (bottom) monolayers. The data are the same as that plotted in Figure 3.

**Table 1**

monolayer	$L_c$ (nN)	$\gamma$ (mJ/m <sup>2</sup> )	$A_c$ (10 <sup>-16</sup> m <sup>2</sup> )	$F_c$ (nN)	$\tau$ (MPa)
FTS	-161 ± 9	143 ± 13	3.5 ± 0.3	4.5 ± 0.2	12.9 ± 1.2
CH <sub>3</sub> -thiol	-68 ± 20	50 ± 21	2.9 ± 0.8	4.0 ± 0.2	13.7 ± 1.5
COOH-thiol	-321 ± 25	449 ± 49	5.5 ± 0.1	10.9 ± 1.2	20.0 ± 1.9

expected for hydrogen bonding between the double-bonded O atom of the COOH group and hydroxyl groups on the glass tip. Assuming  $\sim 21 \text{ \AA}^2$  per molecule surface coverage of the thiols<sup>5</sup> and a similar coverage of OH groups on the bare glass tip, we see that  $\sim 400 \text{ mJ/m}^2$  corresponds to a reasonable hydrogen bond strength of  $\sim 12 \text{ kcal/mol}$ .<sup>18,28</sup> (A water monolayer, if present on the COOH-thiol, is expected to give similar results.) Thus we have a reasonable explanation for the adhesive intermolecular forces acting on the tip for the two thiols. This is not the case for the FTS monolayer. Comparing the FTS and CH<sub>3</sub>-thiol data in Table 1, we see that the work of adhesion is much greater for the FTS. It should be approximately the same, if only van der Waals forces are effective for the fluorocarbon–tip interaction. Indeed, recent AFM experiments have reported no difference in adhesion between CF<sub>3</sub>- and CH<sub>3</sub>-terminated thiols and a SiN tip, although much larger friction forces were observed for the fluorinated tail group.<sup>43</sup> The large value of  $\gamma$  for the FTS

monolayer may be due to incomplete coverage with subsequent water contamination. Another possibility is a dipole–dipole interaction between the electronegative fluorines and the hydroxyl groups on the tip (i.e., a weak hydrogen bond). Clearly, more systematic studies, including tip functionalization, are required to understand this discrepancy.

Another unexpected and perhaps illuminating result is that the large differences in adhesive energies among the two thiols and the FTS are only mildly carried over to the respective shear strength values. We note, however, that the absence of data in the repulsive contact regime for the COOH-thiol due to the strong potential well of the adhesive interaction could mean that the JKR fit provides only a lower bound to the estimated shear strength. At this time, there is no well-established relationship between shear strength and adhesion, yet it is evident from our data that the friction force is highly sensitive to adhesive energies. Much of what determines  $\tau$  may be due to the structural and dynamical properties of the monolayers.

In the initial negative load regime prior to repulsive contact, which is available to us because of our mechanically stable displacement-controlled approach, we see some deviation from the JKR fits. The JKR model assumes that the interfacial forces have zero spatial range, which is appropriate only for short-range forces. Thus it is clear that the negative load regime is not predicted for approaching surfaces by the JKR model. Long-range interactions are included in the alternative Derjaguin–Muller–Toporov model;<sup>44</sup> however, this model predicts zero contact area at the critical load, which is incorrect for our data. Recent models<sup>22</sup> which allow a small, finite range to these forces predict that contact is first made with the surface displaced significantly upward under tensile stress from its equilibrium position; the resulting friction–load relations resemble those depicted in Figure 8. Indeed, observing finite friction with such negative loads indicates that the materials have made contact under tensile stress and thus the “range” of adhesive forces should take account of film deformation as the molecules extend upward in response to the attractive forces.

## Conclusions

In summary, we have shown that the molecular origins of friction can be examined in detail with a novel instrument which features decoupled lateral and normal force sensors, and allows the complete adhesive interaction between tip and surface to be examined without jump-to-contact instabilities. Correlation of normal forces with lateral shear forces reveals both the adhesive and repulsive nature of friction between the contacting surfaces. We have been able to observe the simultaneous onset of friction and adhesive forces, and show that chemical modification of the surface dramatically changes those forces. The displacement range of the adhesive interaction observed in experiments on self-assembled model lubricants suggests significant molecular reorientation and tensile molecular compliance. Thus, energy dissipation, which steeply increases with adhesive forces, can be attributed to tensile molecular deformation, collective molecular chain motion, and dissipative hydrogen-bond ruptures under tensile stress. We have shown that selective area imaging under shear force feedback in the tensile regime allows one to map adhesive forces with the IFM sensor.

(43) Kim, H. I.; Koini, T.; Lee, T. R.; Perry, S. S. *Langmuir* **1997**, *13*, 7192.

(44) Derjaguin, B. V.; Muller, V. M.; Toporov, Y. P. *J. Colloid Interface Sci.* **1975**, *53*, 314.



This is an advantage over AFM-based chemical force microscopy which detects lateral forces while in repulsive contact. Finally, modeling of the friction-load relation within the JKR formalism allows us to see that the tip-surface interaction can be understood as a single asperity contact, and it allows us to quantify the work of adhesion and shear strength. However, limitations to the model due to finite-range adhesive forces and modes of deformation unique to molecular films will require future study. Continuum mechanics can only be used as guide to the behavior we observe. Specific modes of molecular deformation could likely be identified by using approaches such as molecular dynamics modeling.

**Acknowledgment.** R.W.C. acknowledges support from the Natural Sciences and Engineering Research Council of Canada. Sandia is a multiprogram laboratory operated by Sandia Corp., a Lockheed Martin Co., for the United States Department of Energy under Contract DE-AC04-94AL85000.

### Appendix

Following previous treatments,<sup>34,45,46</sup> the vibrating glass tip can be modeled with a damped harmonic oscillator, which has the equation of motion given in eq A1:

$$m\ddot{y} + R\dot{y} + ky = F_0 e^{j\omega t} \quad (\text{A1})$$

In eq A1, the effective mass of the vibrating fiber is  $m$ , the spring constant is  $k$ , the driving force is  $F_0$  with frequency  $\omega$ , and the damping coefficient is given by  $R$ . A solution to eq A1 is

$$y = Ae^{j(\omega t - \theta)} \quad (\text{A2})$$

where  $A$  is the amplitude of the displacement  $y$  and  $\theta$  is the phase lag between the drive force and the displacement. It can be shown that

$$A = \frac{F_0}{[(k - m\omega^2)^2 + (\omega R)^2]^{1/2}} \quad (\text{A3})$$

$$\tan \theta = \frac{\omega R}{k - m\omega^2} \quad (\text{A4})$$

The maximum amplitude  $A_{\max}$  at the oscillator resonance frequency  $\omega_r$  is

$$A_{\max} = \frac{F_0}{R \left[ \left( \frac{k}{m} \right) - \left( \frac{R^2}{4m^2} \right) \right]^{1/2}} \quad (\text{A5})$$

where

$$\omega_r = \left[ \frac{k}{m} - \frac{R^2}{4m^2} \right]^{1/2} \quad (\text{A6})$$

If  $k/m \gg R^2/4m^2$ , then  $A_{\max}$  can be approximated by

$$A_{\max} \cong \frac{F_0}{R[k/m]^{1/2}} = \frac{F_0 Q}{k} = A_{\text{piezo}} Q \quad (\text{A7})$$

where  $A_{\text{piezo}} = F_0/k$  is the piezo drive amplitude (1.23 nm/V for our Stavely Sensors EBL 1 tube),  $Q = m\omega_0/R \gg 1$  is

the quality factor, and  $\omega_0 = (k/m)^{1/2}$  is the natural, undamped resonance frequency. Thus, given the piezo-electric specifications and the measured  $Q$ , which is equal to the full width of the amplitude resonance at  $A_{\max}/\sqrt{2}$ , the tip displacement at resonance can be estimated from eq A7. Absolute measurements of the tip displacement support this approximation.<sup>47</sup>

Taking the real (steady state) part of eq A2, we have for the fiber displacement  $y$

$$y = A \cos(\omega t - \theta) \quad (\text{A8})$$

The total damping (shear) force  $F_s$ , including both external and internal stresses, experienced by the fiber is given by

$$F_s = R\dot{y} = -RA\omega \sin(\omega t - \theta) = RA\omega \cos(\omega t - \theta + \pi/2) \quad (\text{A9})$$

At resonance, the time-averaged damping force is then roughly

$$F_s \cong RA_{\max}\omega_0 = \frac{A_{\max}\omega_0^2 m}{Q} = \frac{A_{\max}k}{Q} \cong A_{\text{piezo}}k \quad (\text{A10})$$

which is constant for a given driving force and is equal to the sum of the internal shear forces within the fiber ( $F_{\text{int}}$ ) and the friction ( $F_f$ ) due to the interaction of the tip with the sample. Thus, as  $F_f$  increases, both  $A_{\max}$  and  $Q$  decrease proportionally to maintain a constant  $F_s$ , which has been verified experimentally.<sup>45</sup> (From the above, one also sees that  $A_{\max}$  and  $Q$  are both proportional to  $1/R$ .) For a velocity-dependent damping force (where there are no force gradients), the resonance frequency will remain unchanged, provided  $k/m \gg R^2/4m^2$ . (In tapping mode AFM there is a large force gradient; thus the cantilever experiences a frequency shift.<sup>12,48</sup>) Since  $A_{\max}$  decreases with increasing  $F_f$ , the detected signal  $V \propto A_{\max}$  decreases, as does  $F_{\text{int}}$ . Thus we may estimate  $F_f$  from eq A11, where  $V_0$  is the signal when the tip is not in contact with the surface:

$$F_f = F_s \left( 1 - \frac{F_{\text{int}}}{F_s} \right) \cong A_{\text{piezo}}k \left( 1 - \frac{V}{V_0} \right) \quad (\text{A11})$$

Thus the quantity  $(1 - V/V_0)$  is directly proportional to the friction (shear force) at the tip, and values for  $F_f$  can be estimated from  $A_{\text{piezo}}$  and  $k$ .  $A_{\text{piezo}}$  is known for a given drive amplitude (although piezo constants may vary with drive amplitude), and the spring constant  $k$  can be calculated from the dimensions and material parameters of the glass fiber.<sup>41</sup> The spring constant will be affected somewhat by the taper of the tip;<sup>49</sup> however, we assume for the present work a single value of  $k$  for the whole fiber. We estimate  $k \cong 150$  N/m and  $A_{\text{piezo}} = 0.12$  nm (for 100 mV drive); thus  $F_f \cong 18$  nN at 100% signal attenuation.

To understand the close correlation between the phase shift and the amplitude damping shown in Figure 2, we rewrite eq A4 as

$$\tan \theta = \frac{\omega R}{m(\omega_0^2 - \omega^2)} = \frac{\omega R}{m(\omega_0 - \omega)(\omega_0 + \omega)} \quad (\text{A12})$$

If  $\omega \approx \omega_0$ , and  $Q = m\omega_0/R$ , then

(45) Karrai, K.; Grober, R. D. *Appl. Phys. Lett.* **1995**, *66*, 1842.  
(46) Yang, Y. T.; Heh, D.; Wei, P. K.; Fann, W. S.; Gray, M. H.; Hsu, J. W. P. *J. Appl. Phys.* **1997**, *81*, 1623.

(47) Wei, C.-C.; Wei, P.-K.; Fann, W. *Appl. Phys. Lett.* **1995**, *67*, 3835.  
(48) Brandsch, R.; Bar, G.; Whangbo, M.-H. *Langmuir* **1997**, *13*, 6349.  
(49) Wei, P. K.; Fann, W. S. *J. Appl. Phys.* **1998**, *83*, 3461.

$$\tan \theta \approx \frac{\omega R}{m(\Delta\omega)(2\omega_0)} \approx \frac{\omega_0}{2Q(\Delta\omega)} \quad (\text{A13})$$

At resonance the phase shift between the drive force and the displacement is close to  $90^\circ$ , and  $\tan \theta \rightarrow \infty$ . However, if the phase shift is measured by the lock-in amplifier in quadrature ( $\theta = 90^\circ$ ), then we have the situation where the measured phase shift is zero before

the tip encounters the surface, and it slowly increases from zero as the tip is damped. Since  $\tan \theta \cong \theta$ , for  $\theta < 20^\circ$ , we see that  $\theta$  is inversely proportional to  $Q$ . We saw in eq A10 that  $Q$  and  $A_{\max}$  decrease proportionally as  $F_f$  increases; therefore, we expect to see a direct correspondence between  $\theta < 20^\circ$  and the amplitude.

LA981521R